AGU PUBLICATIONS

JGR

Journal of Geophysical Research: Atmospheres

RESEARCH ARTICLE
10.1002/2014JD021812

Key Points:
- Fidelity of RCM is comparable if forced with NCEPR2 or ERA40 global reanalysis
- 20CR configurations have poor fidelity owing to amplified transient moisture fluxes
- Convection scheme modulates phase of diurnal max strongly in nonwinter months

Supporting Information:
- Readme
- Figure S1
- Figure S2
- Figure S3

Correspondence to:
C. Selman,
cms05j@my.fsu.edu

Citation:
Selman, C., and V. Misra (2015), Simulating diurnal variations over the southeastern United States, *J. Geophys. Res. Atmos.*, *120*, 180–198, doi:10.1002/2014JD021812.

Received 24 MAR 2014
Accepted 10 DEC 2014
Accepted article online 13 DEC 2014
Published online 13 JAN 2015

Simulating diurnal variations over the southeastern United States

Christopher Selman[1,2] and Vasubandhu Misra[1,2,3]

[1]Department of Earth, Ocean and Atmospheric Science, Florida State University, Tallahassee, Florida, USA, [2]Center for Ocean-Atmospheric Prediction Studies, Florida State University, Tallahassee, Florida, USA, [3]Florida Climate Institute, Florida State University, Tallahassee, Florida, USA

Abstract The diurnal variations from a high-resolution regional climate model (Regional Spectral Model; RSM) are analyzed from six independent decade long integrations using lateral boundary forcing data from the National Centers for Environmental Prediction Reanalysis 2 (NCEPR2), European Center for Medium-Range Weather Forecasts 40-year Reanalysis and the Twentieth Century Reanalysis (20CR). With each of these lateral boundary forcing data, the RSM is integrated separately using two convection schemes: Relaxed Arakawa-Schubert and Kain-Fritsch. The results show that RSM integrations forced with 20CR have the least fidelity in depicting the seasonal cycle and diurnal variability of precipitation and surface temperature over the Southeastern United States. The remaining four model simulations show comparable skill. The differences in the diurnal amplitude of rainfall during the summer months of the 20CR forced integration from the corresponding NCEPR2 forced integration, for example, is found to be largely from the transient component of the moisture flux convergence. The root mean square error (RMSE) of the seasonal cycle of precipitation and surface temperature of the other four simulations (not forced by 20CR) were comparable to each other and highest in the summer months. But the RMSE of the diurnal amplitude of precipitation and the timing of its diurnal zenith were largest during winter months and least during summer and fall months in the four model simulations (not forced by 20CR). The diurnal amplitude of surface temperature in comparison showed far less fidelity in all models. The phase of the diurnal maximum of surface temperature however showed significantly better validation with corresponding observations in all of the six model simulations.

1. Introduction

In the Southeastern United States (SEUS), diurnal variation of precipitation accounts for nearly 40% of the total seasonal variation in the summer [*Bastola and Misra,* 2013]. In fact, the diurnal variation of rainfall is a considerably strong and persistent feature of SEUS climatology [*Dai et al.,* 1999]. *Carbone and Tuttle* [2008] claim that the diurnal variability is stronger over the SEUS than in any other region of the contiguous United States. By virtue of these facts, especially when the climatological features of diurnal variations of precipitation are relatively stationary [*Dai et al.,* 1999], it comes as no surprise that the SEUS is climatologically the wettest region of the United States [*Chan and Misra,* 2010].

There is growing evidence that anthropogenic climate change presents itself in diurnal signals of surface temperature, such as the observed warming in daily minimum temperatures [*Zhou et al.,* 2008; *Portmann et al.,* 2008; *Lauritsen and Rogers,* 2012]. *Dai* [1999] noted a reduction in the afternoon precipitation frequency by 5 to 10% per decade, and a rainfall amount reduction of about 2 to 4 mm/decade over the SEUS. Similarly, larger-scale climatological phenomena affected by climate change, such as the North Atlantic Subtropical High, can impart an influence on the diurnal variability of sea breeze circulations [*Li et al.,* 2011; *Misra et al.,* 2011; *Selman et al.,* 2013]. It is the purpose of this paper to assess the fidelity of diurnal variations in temperature and precipitation as produced by multiple simulations of a regional climate model forced by a variety of global reanalysis at the lateral boundaries and two different cumulus parameterization schemes given such relevance of diurnal variations to the current and future climate of the SEUS.

The simulation of diurnal variations of both temperature and precipitation are however one of the outstanding shortcomings of the Atmospheric General Circulation Models (AGCMs) [*Dai et al.,* 1999; *Dai and Trenberth,* 2004; *Slingo et al.,* 2004; *Braganza et al.,* 2004; *Lewis and Karoly,* 2013]. For example, *Lewis and Karoly* [2013]

indicate that the linear trend of diurnal temperature range in the 1951 to 2005 period is underestimated in the CMIP5 models (which is similar to that exhibited by CMIP3) because they overestimate the changes in the maximum temperature. They further attribute these errors to deficiencies in cloud cover and land surface processes. *Dai* [2006] indicated that AGCMs from the CMIP3 project produce very strong diurnal signals over land, attributed to an early wet season onset, and frequent but weak rainfall. There is however a suggestion from many studies that finer resolution models with astute choice of cumulus parameterization scheme can lead to improvement in the diurnal variations of precipitation [*Liang et al.,* 2004; *Lee et al.,* 2007; *Wang et al.,* 2007; *Evans and Westra,* 2012; *Harding et al.,* 2013]. Some studies indicate that the erroneous phase shift of the diurnal cycle of precipitation displayed by the AGCMs can be rectified to some extent by the high resolution offered by regional climate models [*Liang et al.,* 2004; *Chow and Chan,* 2009]. For example, *Dirmeyer et al.* [2012] note that improved diurnal rainfall simulations follow from improved simulation of the mean rainfall rate when resolution is increased.

The errors in the prescribed lateral boundary conditions limit the fidelity of a regional climate model simulation [*Risbey and Stone,* 1996; *Misra et al.,* 2003; *Misra,* 2007]. Therefore, it is important to account for the uncertainty and relative fidelity of the regional model simulation of an important feature as the diurnal variation over the SEUS.

Dirmeyer et al. [2012] noted that while implementation of better cumulus parameterizations can improve simulations of diurnal variations, the improvements exhibit strong regionality. In a related study, *Stefanova et al.* [2012] using the National Centers for Environmental Prediction - Department of Energy Reanalysis 2 (NCEPR2) [*Kanamitsu et al.,* 2002] and the ECMWF 40-year Reanalysis (ERA40) [*Uppala et al.,* 2005] as lateral boundary conditions to an RCM suggested sensitivity to simulation of the diurnal phase and amplitude of precipitation over the SEUS. Similarly, *DiNapoli and Misra* [2012] showed that dynamic downscaling of the Twentieth century global reanalysis (20CR) [*Compo et al.*, 2011] yielded realistic simulations of the inland progression of the sea breeze in panhandle Florida. However, all of these studies lack a systematic analysis of the diurnal variations forced by the various global atmospheric reanalysis and the combined sensitivity to cumulus parameterization schemes.

Diurnal precipitation in the SEUS is driven by a combination of processes with strong subregional dependence. For instance, in coastal regions of the SEUS, sea breezes are drivers of diurnal variability [*Schwartz and Bosart*, 1979; *Biggs and Graves,* 1962; *LeMone,* 1973]. The late afternoon convergence of sea breezes from the eastern and western coastlines of peninsular Florida results in frequent convective systems [*Byers and Rodebush,* 1948; *Gibson and Vonder Haar*, 1990]. In non-peninsular areas, it is the convergence of sea breeze circulation and background winds that produce the convective systems [*Gentry and Moore,* 1954]. The resultant convective systems do not form immediately at the coastline, and convergence is strongest where coastal curvature accentuates sea breeze convergence [*Pielke,* 1974]. In the non-coastal regions of the SEUS, orographic effects represent a sizeable portion of the diurnal variability [*Parker and Ahijevych,* 2007]. Mountain-crossing mesoscale complex systems from the Central United States, in combination with the ample moist air in the region develop and sustain these convective episodes [*Parker and Ahijevych,* 2007]. Additional large-scale drivers of diurnal precipitation include the North Atlantic Subtropical High [*Li et al.,* 2011] which depending on its zonal position (eastward or westward) can suppress daily maximum convection by increasing local subsidence. *Li et al.* [2013] identified a primary driver of warm season precipitation variability to be large-scale moisture transport, primarily impacted by adjustments to the dynamic environment of the Southeast.

The diurnal variation of precipitation is coincident with corresponding variations in ground hydrology. For example, non-runoff precipitation enhances local soil moisture, which may lead to enhancing local soil-moisture/precipitation coupling [*Wei and Dirmeyer*, 2012]. The phase difference between the diurnal variations of precipitation and temperature can impact the partitioning of surface energy of latent and sensible heat fluxes [*Dai and Trenberth,* 2004]. In the SEUS, *Misra and Dirmeyer* [2009] found that evaporation is energy limited both in the winter and summer seasons. Furthermore, evapotranspiration (ET) is a major contributor to the water budget in the SEUS [*Sun et al.,* 2002]. In the SEUS ET also has a diurnal cycle peaking roughly at 1600 UTC [*Liu et al.,* 2005]. This peak in ET is offset from the corresponding observed peak in precipitation (2200 UTC [*Liu et al.,* 2005; *Stefanova et al.,* 2012]).

In this paper, we examine the diurnal variations from 10-year integrations of regional climate model run independently with two different cumulus parameterization schemes and forced with three different global atmospheric reanalysis. In total, in this study we have examined results from 6 different experiments of the regional climate model. The motivation to conduct these experiments is to systematically analyze the sensitivity of the simulated diurnal variations to the choice of the cumulus parameterization schemes and lateral boundary forcing. As pointed out in *Stefanova et al.* [2012], the downscaled seasonal mean precipitation from NCEPR2 and ERA40 showed systematic differences, which were contrary to the corresponding rainfall differences in the two global reanalysis. We have therefore conducted this comprehensive study to understand the influence of the large-scale lateral boundary conditions and convection schemes on the dominant diurnal variations in the southeastern US.

2. Design of Model Experiments

The Regional Spectral Model (RSM) [*Kanamitsu et al.,* 2010] was adopted as the regional climate model for this study. The spatial resolution of the RSM adopted for this study is 10 km grid resolution, with output from the integration stored at hourly intervals. The RSM has demonstrated proficiency at resolving diurnal variations in the SEUS [*Misra et al.,* 2011; *Stefanova et al.,* 2012; *Dinapoli and Misra,* 2012; *Selman et al.,* 2013]. The RSM has a unique feature of scale selective bias correction [*Kanamaru and Kanamitsu,* 2007] that allows us to avoid multiple nesting in going from the relatively very coarse resolution of the global reanalysis (typically 2° resolution) to the target 10 km grid resolution. It is essentially a spectral nudging technique conducted in the wave-number domain to restrict the RSM drift from the large-scale forcing at the largest spatial scales of the regional domain. The RSM uses the NOAH land-surface model [*Ek et al.,* 2003]. The vegetation map is based on the USGS vegetation map reduced to the 12 NOAH types [*Loveland et al.,* 1995], which offers a realistic depiction of land-use over the SEUS.

Of particular importance to this study was the choice of the cumulus parameterization scheme used in the model simulations. Changing convective schemes within a model can produce dramatically different model biases in rainfall [*Meinke et al.,* 2007]. The choice of the convection scheme also has an influence on the magnitude of diurnal variations [*Liang et al.,* 2004]. In a study employing the RSM, *Meinke et al.* [2007] found that use of the Kain-Fritsch convection scheme (KF) [*Kain and Fritsch*, 1993] produced a realistic simulation of diurnal precipitation over the SEUS. Numerous studies employing the RSM have also noted realistic simulations of diurnal precipitation using the Relaxed-Arakawa Schubert scheme (RAS) [*Moorthi and Suarez,* 1992; *Stefanova et al.,* 2012; *Dinapoli and Misra,* 2012]. In order that we may fully understand how this important choice of parameterization impacts results from our model, we choose to compare data from these two convective schemes known for producing realistic simulations of diurnal precipitation. While additional convection schemes are available within the RSM, these two have been employed in prior studies and have been well tested for climate simulations. These convection schemes primarily differ in their closure assumptions, with KF assuming closure based on convectively available potential energy (CAPE) and RAS using a mass flux-based closure scheme. Within RAS, convective clouds stabilize the environment as quickly as convective clouds destabilize the environment, while in KF closure is based on a monotonic increase in mass flux until CAPE is reduced by 90% [*Kang and Hong*, 2008].

Six model integrations were performed over the SEUS over the period spanning January 1st 1989 to December 31st 1999 (Table 1). In order to mitigate errors introduced by model spin-up, the entirety of 1989 is removed from our calculations. The RSM was forced with three different global atmospheric reanalysis packages: the NCEPR2, the ERA40 and the 20CR, which were downscaled to a horizontal resolution of 10 km using the two convective schemes (mentioned above) separately. A brief outline of the three global reanalysis is given in Table 2. Each global reanalysis package features a different choice of assimilated sea surface temperature data over the integration period. There are some similarities between the packages however, for instance both NCEPR2 and 20CR are run using the same horizontal spectral truncation and vertical discretization. Despite this similarity, there is a fundamental difference between the two packages through 20CR's assimilation of surface observations of mean sea level pressure only. Thus diminishing any overlap that may exist between the other reanalysis packages and 20CR. Soil moisture is initialized by interpolating data from the corresponding analysis to the RSM grid.

Table 1. Name of the Conducted Model Experiments Showing the Choice of Convection Schemes and Global Atmospheric Reanalysis Used in Each Experiment

Convection Scheme	20CR	NCEPR2	ERA40
Kain-Fritsch (KF)	20CR-KF	NCEPR2-KF	ERA40-KF
Relaxed Arakawa Schubert Scheme (RAS)	20CR-RAS	NCEPR2-RAS	ERA40-RAS

Figure 1 depicts the domain and vegetation map of our integrations. Further, it also contains five subregions that we believe to be representative of different climatological drivers of diurnal variability. Subregion 1, the Florida Peninsula, has diurnal variability driven primarily by sea-breeze convergence [*Wallace,* 1975]. Subregion 2 is primarily driven by Southerly sea breezes [*Wallace,* 1975], while subregion 3's variability is primarily driven by the interaction of the sea breeze and the sea-breeze-like circulations arising from thermal differences in soil properties [*Wootten et al.,* 2010]. Subregion 4 is in a unique position, as neither sea breeze nor orographic effects directly drive its diurnal variability, given its situation of being far away from inland propagation of sea breezes and distance from the Appalachians. Finally, the fifth subregion has diurnal variability driven primarily by a combination of orographic effects in the eastern portion, and propagating weather systems of the higher latitudes from the central United States [*Parker and Ahijevych*, 2007]. We also consider a sixth region which represents the entire model domain shown in Figure 1. These subregions will be used to assess model sensitivity to lateral boundary conditions. In order to prevent significant bias being introduced into our analysis, the boundary grid cells in which the RSM nudges the solution towards the global reanalysis following *Lehmann* [1993] are removed.

In order to isolate the diurnal signal, Ensemble Empirical Mode Decomposition (EEMD) [*Huang and Wu,* 2008; *Wu et al.,* 2011] was performed on each of the 10-year model integrations for both precipitation and temperature. EEMD is a data adaptive time series analysis tool that does not use any predetermined basis functions as is routinely done in wavelet transforms or Fourier transforms. EEMD seeks to determine the intrinsic modes of oscillations (also called Intrinsic Mode Function [IMF]) in the data on the basis of local scale separation. The IMFs are obtained through a sequential sifting process that involves identifying local extrema (which includes both maxima and minima). These local extrema are connected with a cubic spline to obtain the upper and lower envelopes. As a preliminary step a "component" is obtained from the difference of the data between the local mean of the upper and lower bound envelopes. This procedure is repeated till the two envelopes are symmetric about zero or within a certain pre-determined tolerance to obtain the "component" as the first IMF. The sifting process is said to be complete when the residue computed as the difference of the IMFs from the original data yields a monotonic function containing one internal extremum from which no more IMFs can be extracted. A particular advantage of this technique over other time series analysis tools is that it can isolate frequencies unambiguously, without any leakage from other frequencies. For further details of the methodology the readers are referred to *Wu et al.* [2011]. EEMD was conducted on all RSM simulations and the observations to isolate the diurnal harmonic. It was found that for the model simulation data, a combination of IMF five and six represented the diurnal precipitation signal. IMF four represented the diurnal signal of temperature in the model simulation. In the observed precipitation data, a combination of IMF five and four contained the diurnal signal in precipitation and temperature, respectively.

3. Observational Data

The model simulation precipitation data is verified against hourly NCEP Stage IV [*Lin and Mitchell,* 2005] multi-sensor data. On its native polar-stereographic grid, the resolution of Stage IV is 4 km, however when interpolated to a lat-lon grid the resolution becomes 0.1° x 0.1°. When EEMD is performed to isolate the

Table 2. List of Global Atmospheric Reanalysis Packages Used as Lateral Boundary Conditions for the Regional Climate Model Simulations

Global Reanalysis	Reference Literature	Spectral Truncation	Vertical Levels	Assimilated Sea Surface Temperature
NCEP-DOE R2	*Kanamitsu et al.* [2002]	T62	28	Merged HadISST1.1 [*Rayner et al.*, 2003] and NOAA Oiv.2 SST [*Reynolds et al.*, 2002] (AMIP II SST; *Hurrell et al.* [2008])
ERA40	*Uppala et al.* [2005]	T159	60	HadISST1.1 (1958–1981) [*Rayner et al.,* 2003] and NOAA Oiv.2 SST (1981–2001) [*Reynolds et al.,* 2002]
20th Century Reanalysis	*Compo et al.* [2011]	T62	28	HadISST1.1 [*Rayner et al.,* 2003]

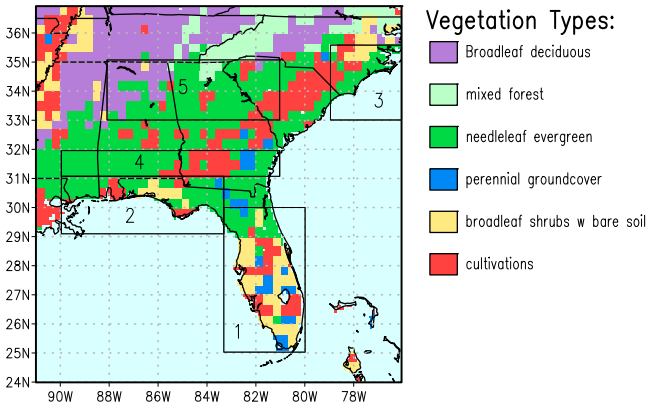

Figure 1. Domain and map of vegetation used in model simulations. Also included are five subregions used for sensitivity analyses.

diurnal signal from the raw data, the resolution is further reduced for the purposes of this study to 0.2° x 0.2° in order to reduce computational time. Numerous past studies have used Stage IV data for validation purposes [*Tian et al.,* 2007; *Davis et al.,* 2003; *Sapiano and Arkin,* 2009] and as such we believe the data to be appropriate for use in this study. Because Stage IV was only made available beginning in 2002, our analysis must span the period 2003–2010. This chosen interval is not coincident with our model integration period. However, *Dai et al.* [1999] noted stationarity in the climatological features of the diurnal variability (which include amplitude, phase and spatial patterns) in regions that displayed strong diurnal variability in precipitation. Furthermore, we are comparing the diurnal climatology across two adjacent decades, and observed trends in diurnal precipitation for the Southeast are small, on the order of a 2 to 4 mm/decade reduction in the rainfall amount [*Dai,* 1999]. As such, between the model simulation and observations, we do not expect the changes in the mean monthly climatology to change significantly. Furthermore, on account of using EEMD to isolate diurnal variability, it is not contaminated by variations at other temporal scales. Consequently the objective of this paper is to verify the climatology of the diurnal variations from the six experiments of decade long simulations conducted with the RSM. The validation data for temperature at hourly interval for the period 1997-2007 comes from the North American Land Data Assimilation System (NLDAS)-1 forcing package [*Cosgrove et al.,* 2003] which has a horizontal resolution of 0.25° by 0.25°. The NLDAS-1 forcing package are assimilated from gauge-based observations and fed into the Eta model-based Data Assimilation System (EDAS) [*Rogers et al.,* 1995] with 3-hourly output, which are temporally disaggregated to one-hourly [*Cosgrove et al.,* 2003].

4. Results

4.1. Seasonal Climatology of Precipitation

Before we proceed to examine the diurnal variations in the various model simulations, we begin with analyzing the seasonal cycle of precipitation. Figure 2 depicts the climatological monthly fraction of total annual precipitation from STAGEIV observations. The coastal regions of the SEUS are characterized by a distinct wet summer season in June, July, and August (Figures 2f–2h) and relatively dry winter months in November, December, and January (Figures 2k, 2l, and 2a). This is generally the opposite for the northwestern portion of the interior, owing to the progression of frontal systems during the winter, spring and fall months. The root mean square error (RMSE) of the climatological monthly fraction from the various model integrations is shown in Figure 3. It is seen that over all months, 20CR-KF simulations exhibit highest RMSE (Figure 3). The RMSE in the monthly fraction of rainfall in 20CR-KF is rather severe in the winter and summer months. This large RMSE in 20CR-KF is followed by those exhibited in 20CR-RAS simulation in the majority of the months. The other 4 simulations are far more comparable in terms of this metric (Figure 3). In summary these results suggest that the seasonal cycle of precipitation in the regional model simulations over the SEUS is relatively more sensitive to the prescribed large-scale conditions of 20CR than the two cumulus parameterization schemes and the other two remaining global reanalysis forcing used in this study.

To illustrate the spatial distribution of the monthly fraction of precipitation, Figure 4 shows results from the NCEPR2-KF simulation, which was one of the better configurations of the regional climate model (see Figure 3). For synthesizing the results, we hereafter consider NCEPR2-KF as our baseline integration, which helps us in comparing the rest of the simulations with this integration. The NCEPR2-KF in Figure 4 generally exhibits a wet bias (in comparison to Figure 2) throughout the year for most of the regional domain with the exception in February, May, November and December (Figure S1 in supporting information) when the simulation seems to exhibit a dry bias outside Florida peninsula. Despite this model bias, the contrast of the wet (Figures 4j–4l) and dry

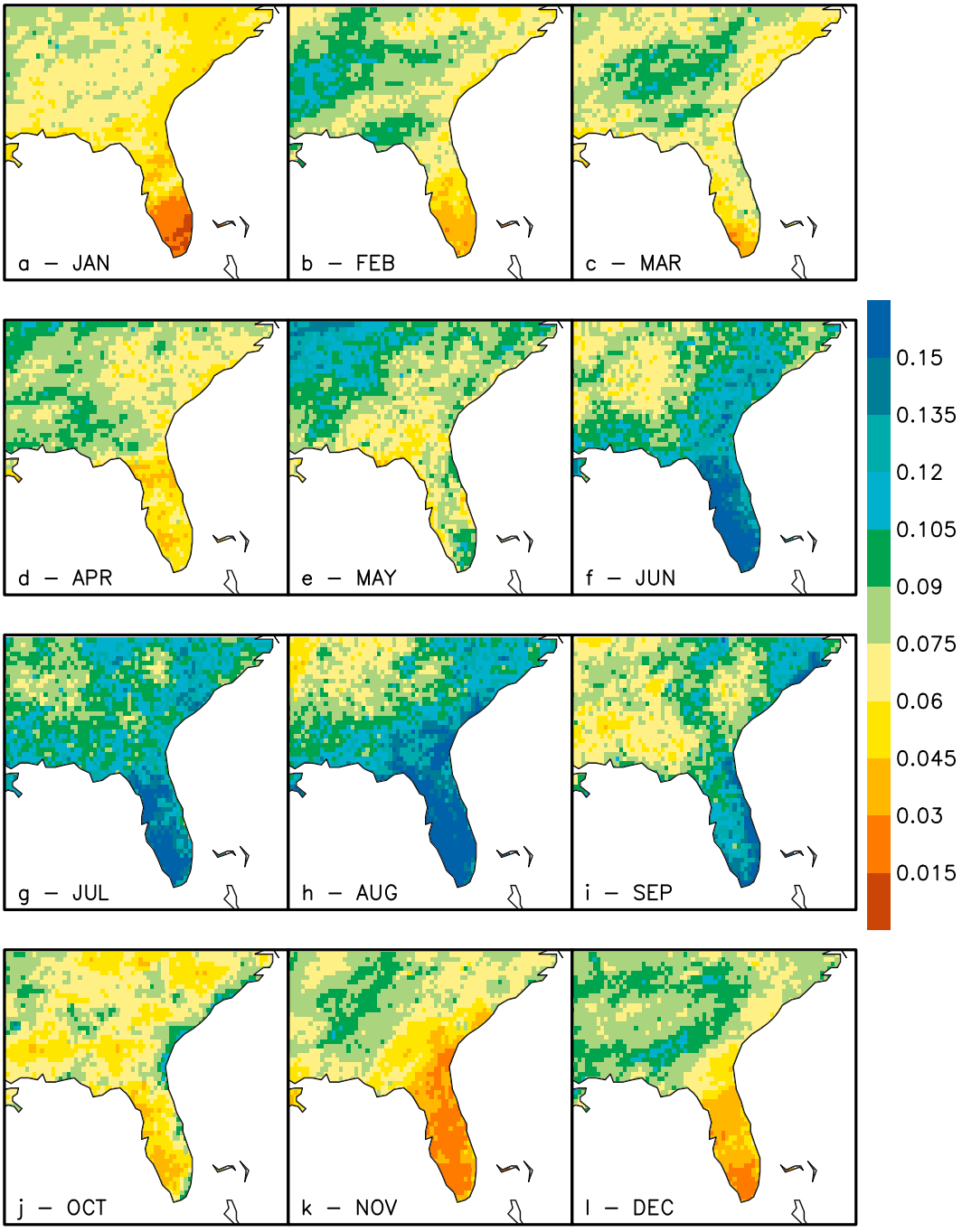

Figure 2. The fraction of the annual total precipitation for the months of (a) January, (b) February, (c) March, (d) April, (e) May, (f) June, (g) July ,(h) August, (i) September, (j) October, (k) November, and (l) December from STAGEIV observations (unitless).

(Figures 4f–4i) seasons is reasonably well represented in the model simulation. In comparison, the transition season of spring (Figures 4c–4e) shows a larger bias with respect to the corresponding observations (Figures 2c–2e). The biases we see in the winter and transition seasons most likely stem from their comparatively smaller observed contribution of diurnal amplitudes (as seen in Figures S1a–S1c; S1j–S1l.) In these periods, especially January and March (Figures S3a and S3c), RSM produces a diurnal amplitude that is too strong (Figures S2a–S2e). However in November (Figure S3k) and Dec (Figure S3l) it is too weak relative to observations (Figures S2k and S2l). In reality, seasonal means over the winter and transition periods are dictated by transient systems as opposed to the stationary component of the diurnal variations.

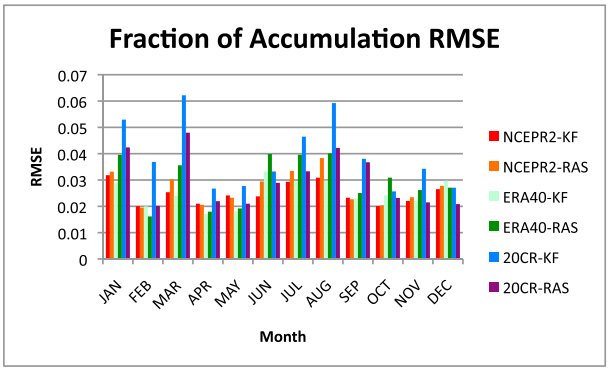

Figure 3. The domain wide RMSE of the climatological fraction of monthly rainfall from the six regional model integrations (unitless).

4.2. Diurnal Variation of Precipitation

After extracting diurnal signals in precipitation and temperature (using the EEMD approach) from the downscaled simulations, monthly averaged diurnal amplitudes in precipitation and temperature were calculated. Because of disparate resolutions of the RSM simulations and the validation data, we used a bilinear interpolation technique in order to fit our model data onto our observed data's grids. We show the climatological mean errors in the diurnal amplitude of precipitation from the NCEPR2-KF simulation (Figure 5). In this figure we have masked out the differences where they are larger than the standard error of the observed mean diurnal amplitude. The peak of the isolated diurnal harmonic averaged for the month determines the mean monthly amplitude in Figure 5 for both observations and model simulations. In Figure 5 we also overlay the timing of the maximum precipitation as a vector, with southerlies being 0000 UTC, southwesterlies being 0300 UTC and so on.

NCEPR2-KF simulates diurnal precipitation amplitude quite poorly in January (Figure 5a), similar to all other configurations (not shown). But the simulation improves significantly in the subsequent months of the year especially in late spring (May), summer and fall seasons when the observed diurnal variations become significant. This improvement is directly related to the strengthening of the diurnal pattern through the wet season, a feature the RSM has been noted to capture well [*Stefanova et al.,* 2012]. The phase of the diurnal peak is also poorly simulated in the winter months (Figures 5a–5c) with differences in the phase being of the order of 6 hours in some parts of the domain. Progressing into the warm season, the NCEPR2-KF configuration begins to simulate the diurnal phase of maximum precipitation reasonably well with domain wide biases on the order of one to two hours. The bias in the timing of the maximum precipitation in the transition seasons of spring (Figures 5c–5e) and fall (Figures 5i–5k) seasons is somewhere between 2-6 hours.

Figure 6 shows the region wide aggregated RMSE of the diurnal amplitude for all the conducted model runs. It is obvious from Figure 6 that RMSE is significantly higher in 20CR-RAS and 20CR-KF in nearly all months, while the rest of the model simulations seem to display far more comparable RMSE. It should be however noted that observed diurnal variations over the SEUS in the winter and spring months are significantly lower than the rest of the year [*Bastola and Misra,* 2013]. The monotonic decrease in RMSE from the summer months to December likely stems from the model's ability to simulate well the strong diurnal pattern of precipitation in the wet season. An interesting aspect in Figure 6 is the abrupt increase in RMSE from Dec. to Jan. across all six model integrations. This stems from two reasons - One, the observed seasonal cycle in Figure S2 exhibits a similar discontinuity with significant weakness in diurnal variation across the domain in Jan relative to Dec. Second, the RSM simulations show similar discontinuity in the seasonal cycle of diurnal variations of precipitation but with December being significantly weaker than January.

4.3. Diurnal Variation of Surface Temperature

We also investigated how sensitive the simulations of diurnal amplitude and phase of surface temperature are in the various model simulations of this study. Similar to Figure 5, Figure 7 shows the climatological monthly mean error in the diurnal amplitude of the surface temperature from the NCEPR2-KF simulation overlaid with vectors representing the climatological time of observed and simulated maximum surface temperatures. A rather sobering result of this analysis in Figure 7 is that the diurnal amplitude error in surface temperature in our baseline NCEPR2-KF integration is larger than the standard error of the observed diurnal amplitude in the winter and fall seasons outside of peninsular Florida. However, the climatological diurnal amplitude error in the NCEPR2-KF (Figure 7) recovers in mid-spring and sustains it through the early fall season. It is however possible that the discrepancy in the model simulations of the diurnal amplitude of the surface temperature is also being seen as a result of the differences in the resolution of the observations and the simulations, which can easily reflect in the elevations of the topography used in the ~28 km grid

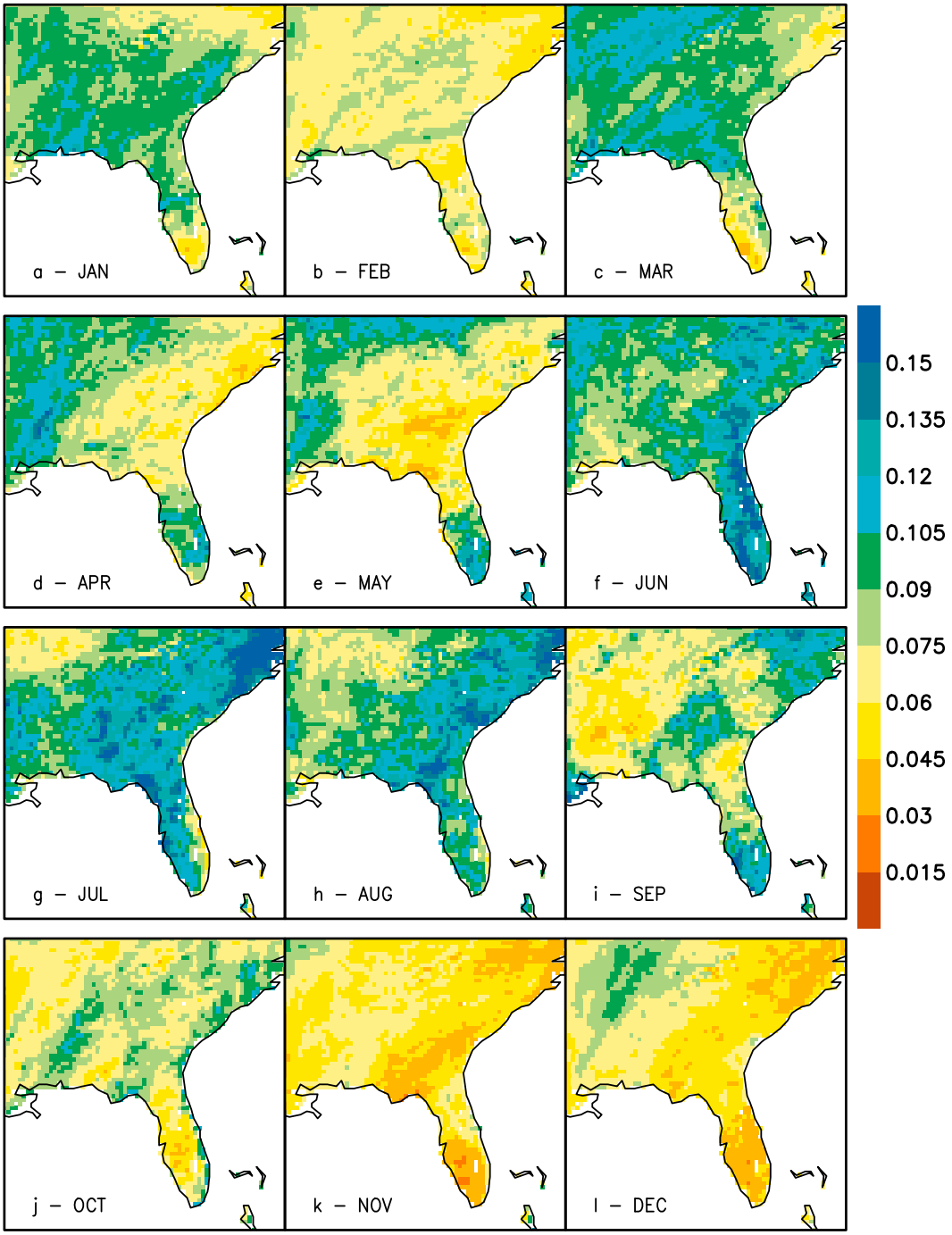

Figure 4. As in Figure 2, but for NCEPR2-KF (unitless).

resolution of the NLDAS-1 assimilation model. Furthermore, the diurnal range of precipitation produced by NLDAS-1 poorly validates with independent observation. As a result, there is scope to speculate of a potential bias in the diurnal energy budget present within the NLDAS-1. This suspicion gets further raised when we notice that despite these amplitude errors the model performs comparably far better at simulating the climatological time of diurnal maximum surface temperature throughout the year (Figure 7). This result is in stark contrast to the results seen in diurnal precipitation, in which months with well-simulated times of maximum rainfall also had the smallest errors in simulated amplitudes. It is also possible that the chosen parameterizations have inherent shortcomings with respect to diurnal ranges of temperatures. The largest

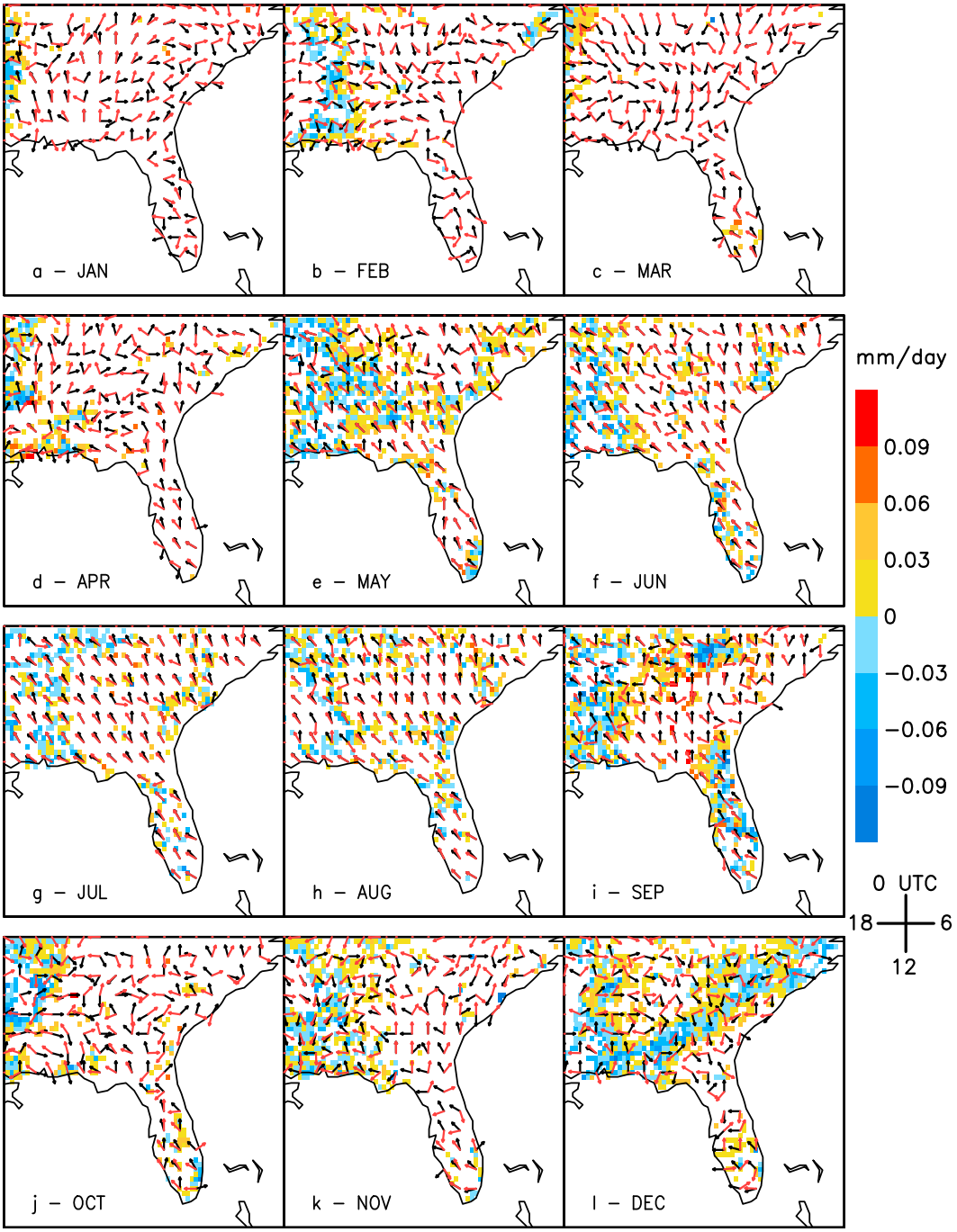

Figure 5. The climatological diurnal amplitude error (mm d^{-1}) of NCEPR2-KF. The values of these errors are masked out when they exceed the standard error of the observational mean diurnal amplitude. The overlaid vectors denote the simulated (red) and observed (black) time of maximum precipitation. Southerly vectors denote 0000 UTC, westerly 0600 UTC, and so on. When only one of the vectors is seen, then simulation and observation timing are coincident.

biases are on the order of one hour in coastal areas and around the Appalachians. Figure 8 shows the aggregate RMSE of the diurnal amplitude of the surface temperature over the whole domain from all model integrations. We again note that 20CR configurations produce the highest RMSE throughout the year (likely owing to large-scale biases from the lateral boundary which is discussed in the conclusions.) We also see that 20CR-RAS performs comparably to other configurations in the summer, when diurnal variations in rainfall are most pronounced.

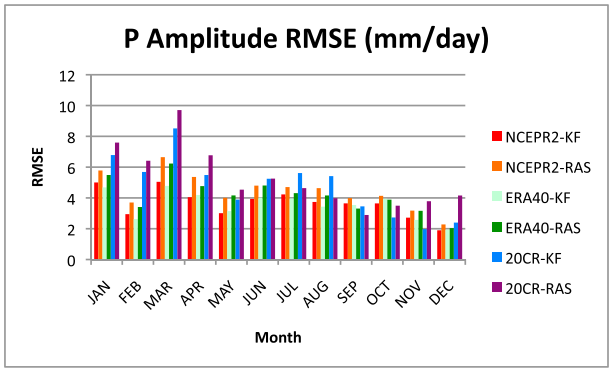

Figure 6. The domain wide RMSE of the simulated diurnal precipitation amplitude from all six model integrations.

4.4. Sensitivity

In summary our analysis so far indicates that the climatological diurnal variations of the precipitation and surface temperature in the model integrations forced by 20CR are significantly different (and inferior) to all other model integrations. Furthermore, when excluding 20CR simulations, distinguishing the relative fidelity of the diurnal variations of the surface temperature and precipitation from the other four model integrations produces results that are inconclusive.

In order to understand how changing the lateral boundary conditions and convection scheme impacted the diurnal variation of the regional climate model simulations, we objectively computed sensitivity (S; Figures 9–11) with respect to the baseline model integration as:

$$S = \left| \frac{(V_b - V)}{(V_b - V_{obs})} \right|, \tag{1}$$

where, V could be any one of the three variables: diurnal amplitude of precipitation, diurnal amplitude of surface temperature, phase of diurnal maximum of precipitation from any of the five model runs besides the baseline integration, V_b and V_{obs} are the corresponding variable from the baseline integration and observations respectively. In other words, S is the fraction of the relative change of the variable in question between two model integrations with respect to the corresponding departure of the baseline experiment from the observations of the variable. For the purposes of this discussion, we are interested in seeing how model simulations change under differing configurations. Since S can have a wide range of values depending on the fidelity of the simulation, we decided to plot the logarithm of S to capture a larger range of its values. This required us to compute its absolute value as shown in equation (1). We computed S as an average for the subregions (outlined in Figure 1), in order that we may assess if our model is more sensitive to lateral boundary forcing and convection scheme under regimes with different drivers of diurnal variability. As noted in section 2, we subdivided our region (see Figure 1) into the Florida peninsula (Region 1), Gulf of Mexico coast (Region 2), Carolina coast (Region 3), non-mountainous interior (Region 4), and mountainous interior (Region 5).

Figure 9 shows the sensitivity of the diurnal precipitation amplitude to lateral boundary forcing and convection scheme. A value of S close to 1 indicated less sensitivity, while large deviations from 1 would suggest high sensitivity. Deviations beyond 50 are not shown in the figure. A value very close to zero would suggest that the experiment integration is better than the baseline integration. Very large values of S would suggest higher fidelity of the baseline integration relative to the experiment integration. 20CR forced RSM experiments appear to have the highest sensitivity values for both KF and RAS as an average, though no one conclusive statement can be made about them as a whole. In the month of February, for instance, subregions 2, 4 and 5 exhibit strong sensitivity to 20CR configurations, but this feature does not persist in March. In June, subregion 1 appears to be extremely sensitive to lateral boundary condition and cumulus parameterization choice, a feature seen only again in September. In most other months, however, it appears that all non-20CR configurations perform similarly over most regions, exhibiting very low sensitivity to configuration. We find that most subregions exhibit sensitivity patterns similar to the region as a whole in the winter and early spring months, when the diurnal amplitude is weaker than the rest of the year in the SEUS,. However in the summer and fall months, the heterogeneity of the various subregions in terms of its topography, vegetation distribution, proximity to coasts, and its geographic location (longitude and latitude) make the sensitivity patterns look more dissimilar to the corresponding pattern for the region as a whole.

Next we examine the sensitivity of the phase of the diurnal maximum in precipitation (Figure 10). In order to prevent artificial bias in the results when precipitation occurs at 2300 UTC in comparison to 0000 UTC, our analysis seeks the minimum difference in time using the 24-hour clock. As in Figure 9 above, we see the

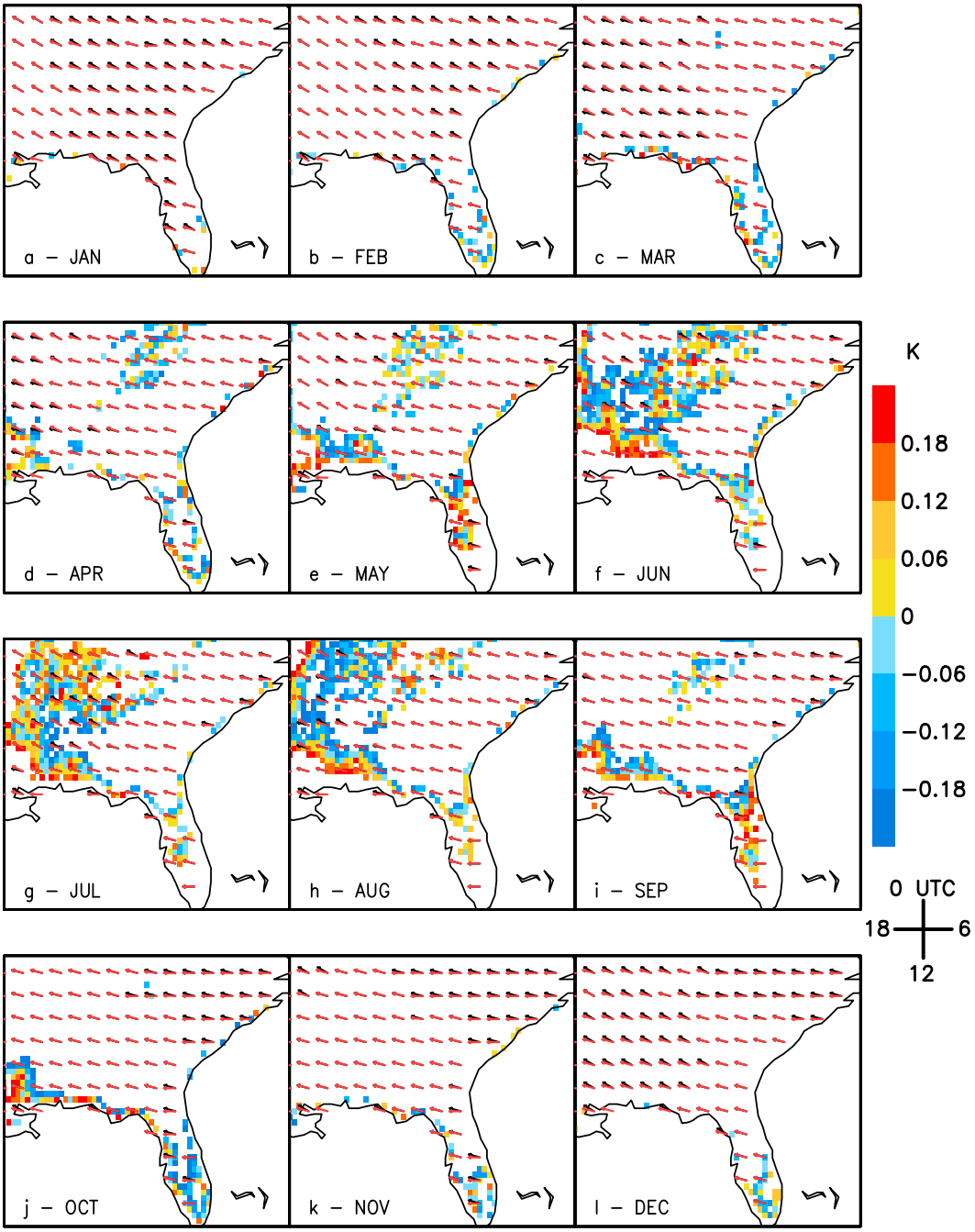

Figure 7. As in Figure 5, but for the diurnal temperature amplitude error (Kelvins) and vectors represent the timing of maximum temperature in NCEPR2-KF simulations (red) and observations (black).

greatest average sensitivity in configurations using 20CR, though again this is not an annual or subregion persistent phenomenon. In the summer months, we see that phase is strongly sensitive to convection scheme choice in subregions 1 and 2. In the spring months of March and April a majority of the subregions demonstrate sensitivity to both changing the convective parameterization and boundary condition. Into November and December it appears that the RSM simulated phase of diurnal precipitation is relatively insensitive to convection scheme and boundary condition choice. As seen in the previous figure, the sensitivity patterns of diurnal phase for the various subregions are similar to that for the whole domain in the winter months. In examining the sensitivity of the amplitude of diurnal amplitude of temperature (Figure 11) we find that for all months, the model is generally insensitive to choice of both lateral boundary conditions

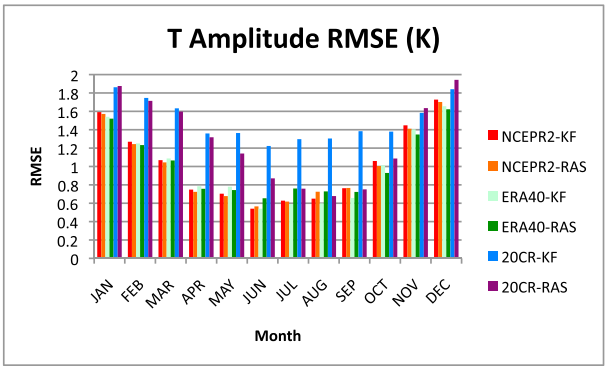

Figure 8. As in Figure 6, but for diurnal temperature amplitude.

and convection schemes, except in isolated cases using 20CR configurations (June, July and August for subregions 3, 4, and 5.) We further note that subregion 3 and 4 also exhibit sensitivity to choice of convection scheme, as ERA40-KF sensitivities are low whilst ERA40-KF RAS sensitivities are high.

4.5. Moisture Budget

In order to understand these sensitivities further we computed the moisture budget for the various regions. We will focus our moisture budget discussion on areas and experiments that displayed some of the highest sensitivity. In August, ERA40-RAS produced high values of sensitivity in the diurnal amplitude of precipitation in subregion 4 when compared to the baseline integration (Figure 9). Again in August, NCEPR2-RAS produced a high value of sensitivity in the diurnal phase of precipitation over subregion 1 (Figure 10). Finally, in September, sensitivity was high when computed against 20CR-KF in subregion 1 (Figure 9). The diurnal variations of each term of the moisture budget for these regions and experiments are shown in Figure 12. The moisture budget equation analyzed for this figure takes the form of:

$$\frac{\partial Q}{\partial t} = -\nabla \cdot M + E - P \tag{2}$$

where,

$$Q = \frac{1}{g}\int_{P_s}^{P_{top}} q dp \tag{3}$$

and

$$\nabla \cdot M = \nabla \cdot m + \nabla \cdot m'. \tag{4}$$

$-\nabla \cdot m$ is defined as the stationary moisture flux convergence,

$$= -\frac{1}{g}\int_{p_s}^{p_{top}} \nabla \cdot \overline{V}\,\overline{q} dp \tag{5}$$

and $-\nabla \cdot m'$ is defined as the transient moisture flux convergence,

$$= -\frac{1}{g}\int_{p_s}^{p_{top}} \nabla \cdot \overline{V}'q' dp \tag{6}$$

with E and P defined as the surface evaporation and precipitation respectively. The transient moisture flux convergence is computed as a residual. It may be noted in Figure 12 that positive (negative) values of $-\nabla \cdot M = (-\nabla \cdot m - \nabla \cdot m')$ represent moisture flux convergence (divergence).

In Figure 12 we see that at the nadir of the diurnal cycle of precipitation, all terms of the moisture budget are small and comparable in all configurations. The largest differences from 0000 UTC to 1200 UTC between the model experiments are in the transient moisture flux convergence and surface evaporation terms. As we approach the diurnal zenith (around 2000 UTC) the moisture budget reveals that there is a moderate increase (decrease) in the vertically integrated stationary moisture flux convergence (local storage) and steep increase in local evaporation, precipitation, and the vertically integrated transient moisture flux divergence in all simulations. In August over subregion 1, comparing these moisture budget terms between the NCEPR2-KF and NCEPR2-RAS we find that the largest differences stem in the transient moisture flux divergence term followed by those in precipitation and evaporation (Figure 12e). This assertion is also true for September in subregion 1 between the NCEPR2-KF and 20CR-KF experiments (Figure 12f). In subregion 4 however, noted for its sensitivity in diurnal precipitation amplitude, the difference in evaporation is small between NCEPR2-KF and ERA40-RAS (Figure 12d). The difference in the transient moisture flux divergence term remains large,

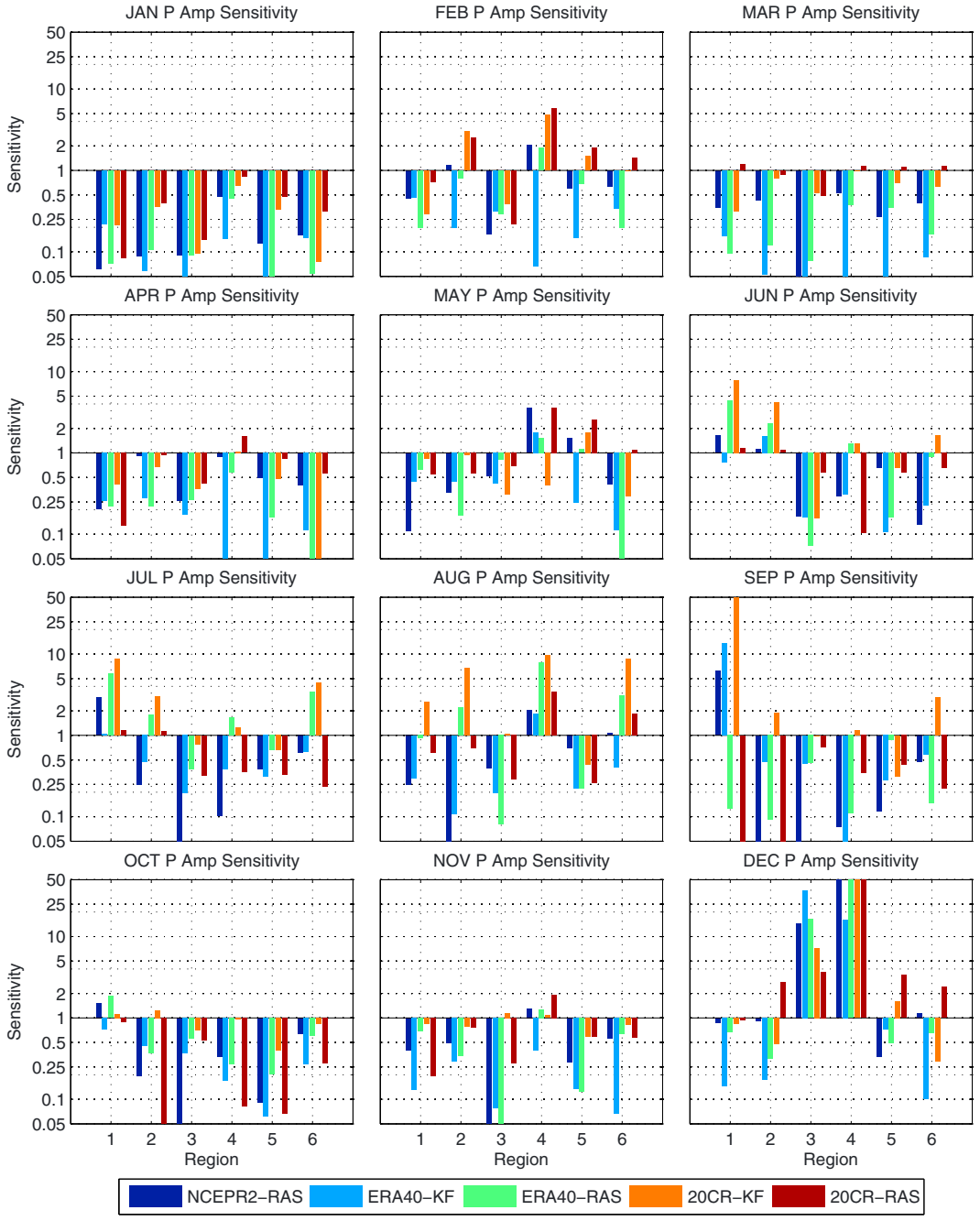

Figure 9. The climatological sensitivity (see text) of the diurnal precipitation amplitude using NCEPR2-KF as the base line integrations for various subregions indicated in Figure 1. Region 6 represents the domain-wide sensitivity.

however, owing to large difference in precipitation. The differences in the local storage of the moisture in the column and the stationary component of the vertically integrated moisture flux convergence are relatively small among all subregions, months and simulations shown in Figure 12. In other words, this budget reveals that the large sensitivity in both the diurnal amplitude and phase of precipitation found between the baseline model integration, NCEPR2-KF, and all other experiments (Figures 9 and 10) could be traced to the differences in the transient moisture flux convergence. The changes in precipitation from the simulations also entail changes in local storage. It is not surprising to note that the stationary components of the moisture flux convergence in the model integrations are comparatively similar. This is because the prognostic variables from the boundary conditions are more likely to be similar in their stationary components than their transient

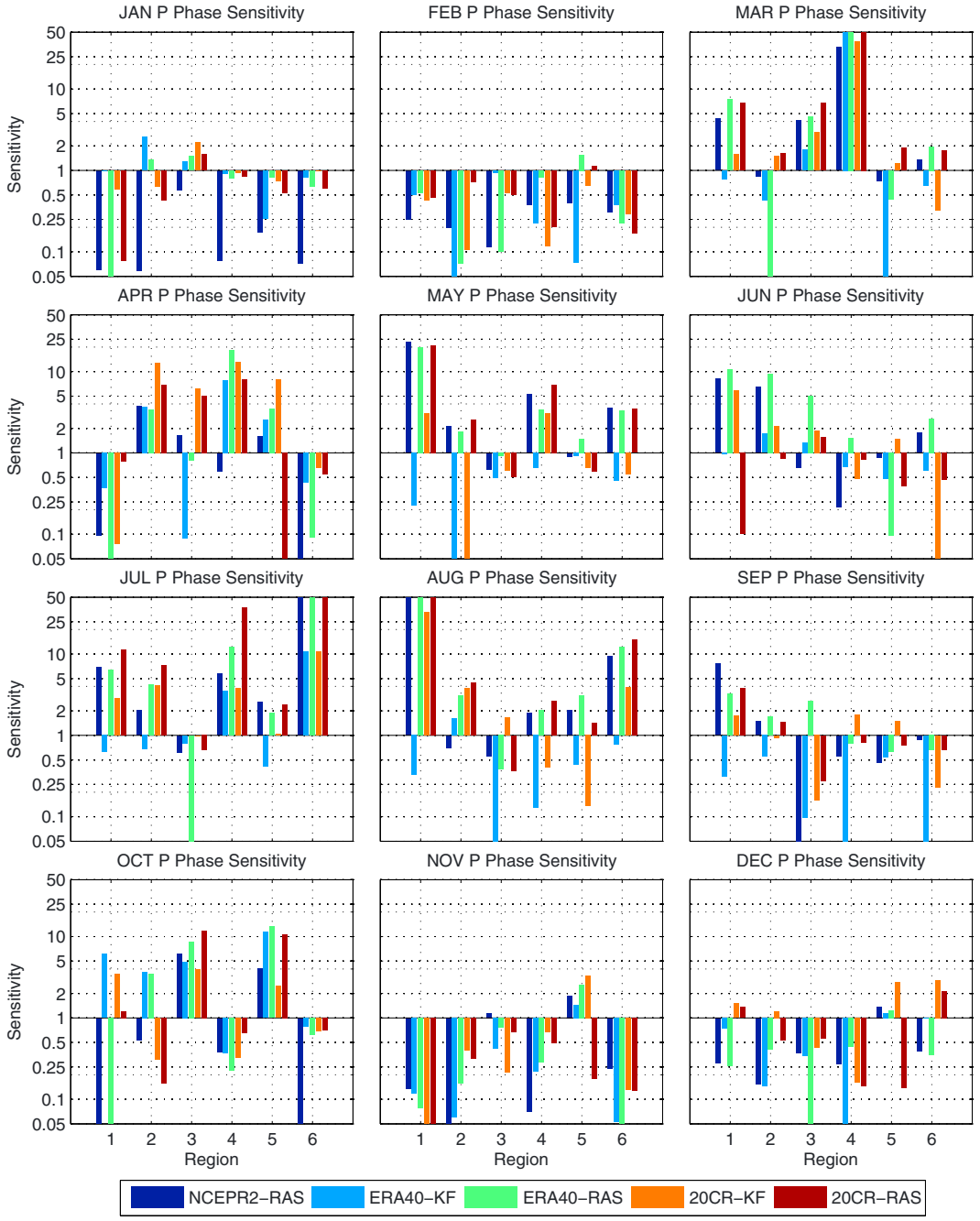

Figure 10. As in Figure 9, but for timing of climatological maximum in diurnal precipitation.

components. The source of these disparities in the transient scale likely stems from the noted propagation of biases from the 20CR reanalysis packages, which include a persistent cold bias along the northern portion of the domain, and warm bias along the gulf coast [*Dinapoli and Misra,* 2012]. Both these features can cause underproduction (overproduction) by stabilizing (destabilizing) the atmosphere in the respective regions and from its impact on the large-scale meridional temperature gradient.

5. Conclusions

The fidelity and sensitivity of regional climate model simulations of diurnal variability of precipitation and surface temperature to changing lateral boundary forcing prescribed from different global reanalysis and

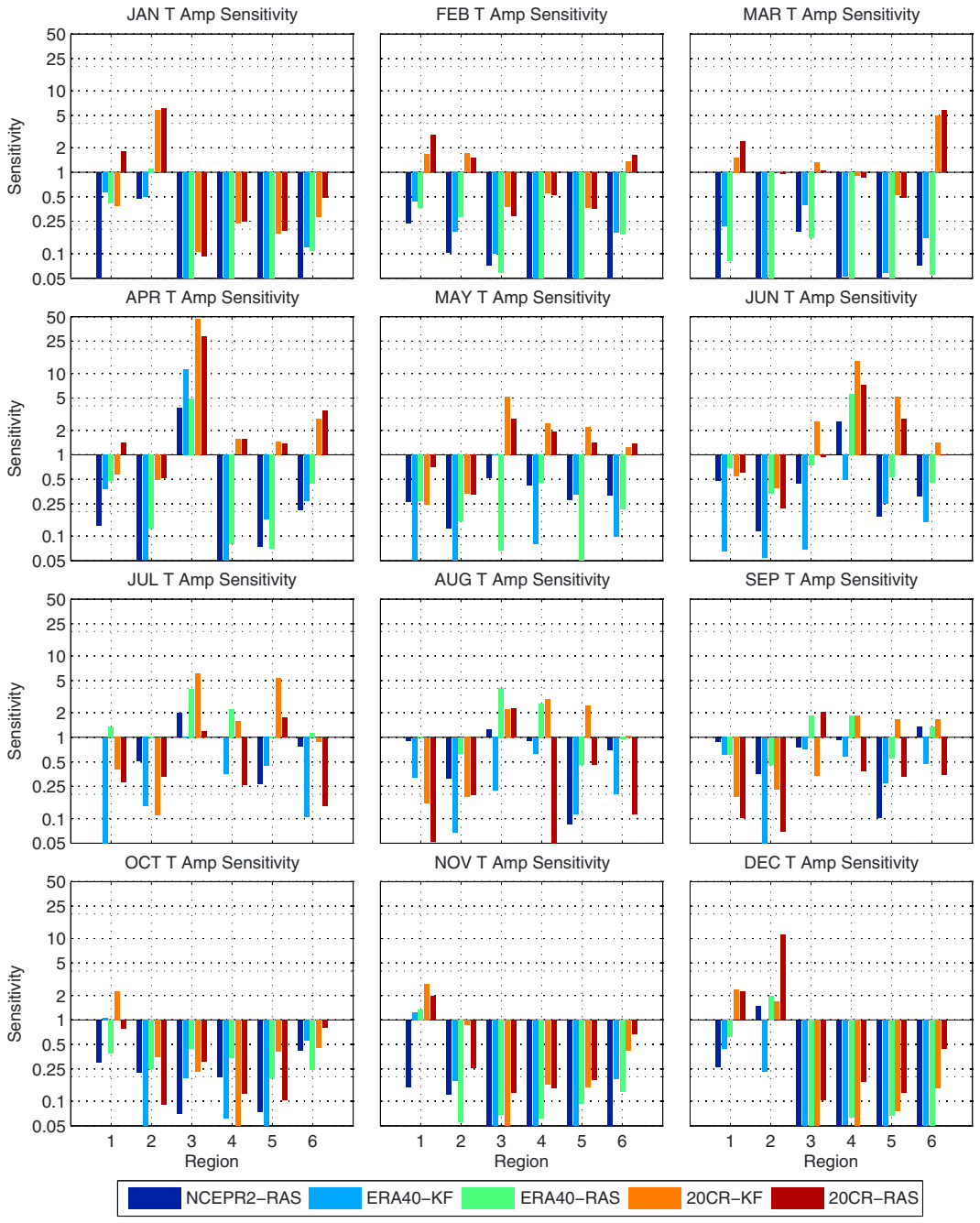

Figure 11. As in Figure 9, but for diurnal temperature amplitude.

convection schemes were examined in this study. In total, we conducted six independent integrations forced with NCEPR2, ERA40, and 20CR global reanalysis and with two different convection schemes, namely, Kain-Fritsch [*Kain and Fritsch,* 1993] and Relaxed Arakawa Schubert scheme [*Moorthi and Suarez,* 1992]. We regarded NCEPR2-KF as our baseline integration for convenience.

The fidelity of the diurnal and seasonal climate variations in precipitation in these regional climate model simulations reveals that configurations forced with 20CR global reanalysis (20CR-KF and 20CR-RAS) show the largest RMSE. The RMSE of the annual cycle of precipitation and surface temperature of the other four simulations (not forced by 20CR) were, however, comparable to each other and highest in the summer months. But the RMSE of the diurnal amplitude of precipitation and the timing of its diurnal zenith were largest during winter months and least during summer and fall months in the four model simulations (not

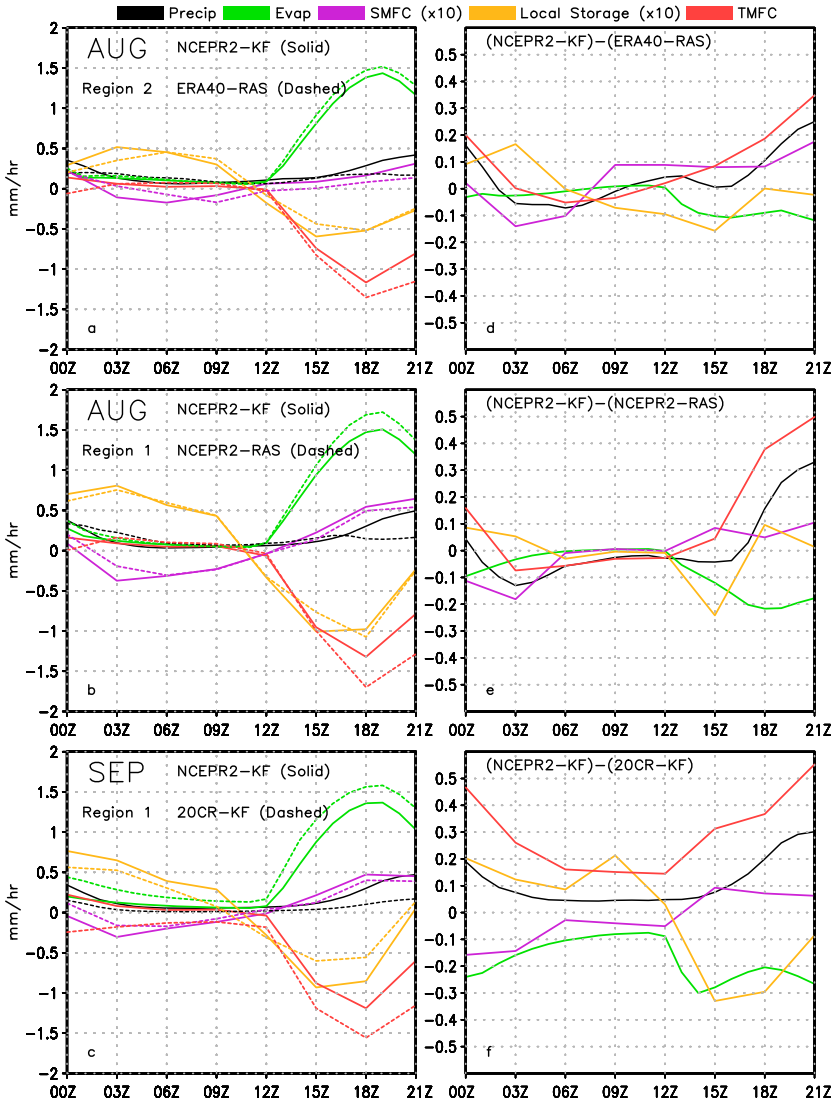

Figure 12. All terms of the moisture budget for (a) August in Region 4, with NCEPR2-KF and ERA40-RAS, (b) August in Region 1 with NCEPR2-KF and NCEPR2-RAS, and (c) September in Region 1 with NCEPR2-KF and 20CR-KF. Vertically integrated and time dependent terms are plotted at 3-hourly intervals. For convenience of comparing the terms in the budget, the stationary vertically integrated moisture convergence (SMFC) and the storage terms are scaled by 10. The transient flux term (TMFC) is computed as a residual of all terms of the moisture budget. (d–f) Difference plots.

forced by 20CR). The diurnal amplitude of surface temperature in comparison showed far less fidelity in all model simulations especially outside of the Florida Panhandle within the SEUS domain. This low fidelity can possibly be attributed to relatively coarse resolution and hence topography of NLDAS-1, biases in diurnal precipitation in the NLDAS-1 suite, and our model's lack of consideration for land use change in the SEUS. In addition, the bias related to cloud cover in the RSM cannot be ignored. *Li and Misra* [2014] find that RSM has a tendency to overestimate the low cloud fraction. The phase of the diurnal maximum of surface temperature shows significantly much higher fidelity in all of the 6 model simulations.

We objectively defined sensitivity as a fraction of the difference between the baseline regional climate model integration (NCEPR2-KF) and each of the other five experiments divided by the difference between the baseline value and observed value of the variable. We found that 20CR-KF was most different from the baseline integration in the simulation of the diurnal amplitude of precipitation, especially in the summer and fall months. In contrast the sensitivity of the phase of the diurnal maximum in precipitation is weak, especially in the winter months, to changes in the lateral boundary conditions and convection schemes. However,

convection schemes seem to modulate the phase of the diurnal maximum in precipitation in the other three seasons more than the boundary conditions. On the other hand, the sensitivity of diurnal amplitude of surface temperature to changes in convection scheme and lateral boundary conditions is comparatively far less. In further examining the cause of the significantly large differences in the diurnal amplitude of the precipitation in the summer months between NCEPR2-KF and 20CR-KF, we find from moisture budget analysis that transient moisture fluxes and surface evaporation exhibited the largest differences between the two simulations. In regions and months with low sensitivity, however, model simulations are in agreement with one another with insignificant difference in transient moisture flux and surface evaporation (not shown).

In conclusion, our study finds that the regional climate model simulation of the diurnal variations of surface meteorology in the SEUS domain seems to be comparable in its fidelity when forced with NCEPR2 or ERA40 global reanalysis using either the Kain-Fritsch or Relaxed Arakawa Schubert scheme. In other words, discerning the differences between the impact of NCEPR2 and ERA40 from changes in convection scheme is inconclusive. The use of 20CR as a lateral boundary condition does however show a significant difference. Further, it does not verify as well as the rest of the model simulations of this study. These results are significant, as projections of climate change can benefit substantially from incorporating considerations for finer-scale features such as the diurnal variation. While capturing variance of extreme events is significant, so too is understanding the changes to stationary patterns like the diurnal variability, which is a significant part of the seasonal variability in the SEUS [*Bastola and Misra,* 2013]. This study is suggesting that by understanding the fidelity of diurnal scale features in the current era from a forced downscaled integration, we may be able to assess the relative reliability of the GCM forcing for future projections of diurnal features in the downscaled integration. At minimum, we will have an enhanced understanding of the individual regional climate model's sensitivity to choice of driving AGCM. This understanding will allow for an improved characterization of our confidence in the projections produced by each regional climate model. In addition to this work, we are currently conducting regional climate model experiments over the SEUS domain with implementation of irrigation and urbanization parameterizations in the NCEPR2-KF configuration, which in our future study will reveal their impacts in modulating the biases shown in this work.

Acknowledgments

This work was supported by grants from NOAA (NA12OAR4310078, NA10OAR4310215, NA11OAR4310110) and USGS G13AC00408. All model integrations for this paper were done on the computational resourced provided by the Extreme Science and Engineering Discovery Environment (XSEDE) under TG-ATM120010. Data used in this study are freely available upon request from the authors via cselman@coaps.fsu.edu or vmisra@coaps.fsu.edu.

References

Bastola, S., and V. Misra (2013), Sensitivity of hydrological simulations of southeastern United States watersheds to temporal aggregation of rainfalls, *J. Hydrometeorol.*, *14*, 1334–1344.

Biggs, W., and M. Graves (1962), A Lake Breeze Index, *J. Appl. Meteorol. Climatol.*, *1*, 474–480.

Braganza, K., D. Karoly, and J. M. Arblaster (2004), Diurnal temperature range as an index of global climate change during the twentieth century, *Geophys. Res. Lett.*, *31*, L13217, doi:10.1029/2004GL019998.

Byers, H., and H. Rodebush (1948), Causes of thunderstorms of the Florida Peninsula, *J. Meteor.*, *5*, 275–280.

Carbone, R. E., and J. D. Tuttle (2008), Rainfall occurrence in the U.S. warm season: The diurnal cycle, *J. Clim.*, *21*, 4132–4146.

Chan, S., and V. Misra (2010), A diagnosis of the 1979–2005 extreme rainfall events in the southeastern United States with isentropic moisture tracing, *Mon. Weather Rev.*, *138*, 1172–1185.

Chow, K. C., and J. C. L. Chan (2009), Diurnal variations of circulation and precipitation in the vicinity of the Tibetan Plateau in early summer, *Clim. Dyn.*, *32*(1), 55–73.

Compo, G. P., et al (2011), The twentieth century reanalysis project, *Q. J. R. Meteorol. Soc.*, *137*, 1–28, doi:10.1002/qj.776.

Cosgrove, B., et al. (2003), Real-time and retrospective forcing in the North American Land Data Assimilation System (NLDAS) Project, *J. Geophys. Res.*, *108*, 8842, doi:10.1029/2002JD003118.

Dai, A. (1999), Recent changes in the diurnal cycle of precipitation over the United States, *Geophys. Res. Lett.*, *26*, 341–344, doi:10.1029/1998GL900318.

Dai, A. (2006), Precipitation characteristics in eighteen coupled climate models, *J. Clim.*, *19*, 4605–4630.

Dai, A., and K. E. Trenberth (2004), The diurnal cycle and its depiction in the Community Climate System Model, *J. Clim.*, *17*, 931–951.

Dai, A., F. Girgi, and K. E. Trenberth (1999), Observed and model-simulated diurnal cycles of precipitation over the contiguous United States, *J. Geophys. Res.*, *104*, 6377–6402, doi:10.1029/98JD02720.

Davis, C. A., K. W. Manning, R. E. Carbone, S. B. Trier, and J. D. Tuttle (2003), Coherence of warm-season continental rainfall in numerical weather prediction models, *Mon. Weather Rev.*, *131*, 2667–2679.

Dinapoli, S., and V. Misra (2012), Reconstructing the 20th century high-resolution climate of the southeastern United States, *J. Geophys. Res.*, *117*, D19113, doi:10.1029/2012JD018303.

Dirmeyer, P. A., et al. (2012), Simulating the diurnal cycle of rainfall in global climate models: Resolution versus parameterization, *Clim. Dyn.*, *39*, 399–418.

Ek, M. B., K. E. Mitchell, Y. Lin, E. Rogers, P. Grunmann, V. Koren, G. Gayno, and J. D. Tarpley (2003), Implementation of Noah land surface model advances in the National Centers for Environmental Prediction operational mesoscale Eta model, *J. Geophys. Res.*, *108*, 8851, doi:10.1029/2002JD003296.

Evans, J. P., and S. Westra (2012), Investigating the mechanisms of diurnal rainfall variability using a regional climate model, *J. Clim.*, *25*, 7232–7247.

Gentry, R., and P. Moore (1954), Relation of local and general wind interaction near the seas coast to time and location of air-mass showers, *J. Atmos. Sci.*, *11*, 507–511.

Gibson, H., and T. Vonder Haar (1990), Cloud and convection frequencies over the southeast United States as related to small-scale geographic features, *Mon. Weather Rev.*, *118*, 2215–2227.
Harding, K., P. K. Snyder, and S. Liess (2013), Use of dynamical downscaling to improve the simulation of central U.S. warm season precipitation in CMIP5 Models, *J. Geophys. Res. Atmos.*, *118*, 12,522–12,536, doi:10.1002/2013JD019994.
Huang, N., and Z. Wu (2008), A review on Hilbert-Huang transform: Method and its applications to geophysical studies, *Rev. Geophys.*, *46*, RG2006, doi:10.1029/2007RG000228.
Hurrell, J. W., J. J. Hack, D. Shea, J. M. Caron, and J. Rosinski (2008), A new sea surface temperature and sea ice boundary dataset for the Community Atmosphere Model, *J. Clim.*, *21*, 5145–5153.
Kain, J., and M. Fritsch (1993), Convective parameterization for mesoscale models: The Kain-Fritsch scheme, *Meteorol. Monogr.*, *24*, 165–170.
Kanamaru, H., and M. Kanamitsu (2007), Scale selective bias correction in a downscaling of global analysis using a regional model, *Mon. Weather Rev.*, *135*, 334–350.
Kanamitsu, M., W. Ebisuzaki, J. Woollen, S. K. Yang, J. J. Hnilo, M. Fiorino, and G. L. Potter (2002), NCEP DOE AMIP II reanalysis (R2), *Bull. Am. Meteorol. Soc.*, *83*, 1631–1643.
Kanamitsu, M., K. Yoshimura, Y. Yhang, and S. Hong (2010), Errors of interannual variability and multi-decadal trend in dynamical regional climate downscaling and its corrections, *J. Geophys. Res.*, *115*, D17115, doi:10.1029/2009JD013511.
Kang, H.-S., and S.-Y. Hong (2008), Sensitivity of the simulated East Asian summer monsoon climatology to four convection parameterization schemes, *J. Geophys. Res.*, *113*, D15119, doi:10.1029/2007JD00969.
Lauritsen, R. G., and J. C. Rogers (2012), U.S. diurnal temperature range variability and regional causal mechanisms, 1901–2002, *J. Clim.*, *25*, 7216–7231.
Lee, M. I., et al (2007), Sensitivity to horizontal resolution in the AGCM simulations of warm season diurnal cycle of precipitation over the United States and Northern Mexico, *J. Clim.*, *20*, 1862–1881.
Lehmann, R. (1993), On the choice of relaxation coefficients for Davies lateral boundary scheme for regional weather prediction models, *Meteorol. Atmos. Phys.*, *52*, 1–14.
LeMone, M. A. (1973), The structure and dynamics of horizontal roll vortices in the planetary boundary layer, *J. Atmos. Sci.*, *30*, 1077–1091.
Lewis, S., and D. J. Karoly (2013), Evaluation of historical diurnal temperature range trends in CMIP5 models, *J. Clim.*, *26*, doi:10.1175/JCLI-D-13-00032.1.
Li, H., and V. Misra (2014), Thirty two year ocean-atmosphere coupled downscaling of global reanalysis over the Intra-American Seas, *Clim. Dyn.*, doi:10.1007/s00382-014-2069-9.
Li, L., W. Li, and A. P. Barros (2013), Atmospheric moisture Budget and its regulation of the summer precipitation variability over the southeastern United States, *Clim. Dyn.*, *41*, 613–631.
Li, W., L. Li, R. Fu, L. Deng, and H. Wang (2011), Changes to the North Atlantic subtropical high and its role in the intensification of summer rainfall variability in the southeastern United States, *J. Clim.*, *24*, 1499–1506.
Liang, X.-Z., L. Li, A. Dai, and K. Kunkel (2004), Regional climate model simulation of summer precipitation diurnal cycle over the United States, *Geophys. Res. Lett.*, *31*, L24208, doi:10.1029/2004GL021054.
Lin, Y., and K. E. Mitchell (2005), The NCEP Stage II/IV hourly precipitation analyses: Development and applications, in *Preprints, 19th Conf. on Hydrology*, Am. Meteorol. Soc., San Diego, Calif., 9–13 Jan., Paper 1.2.
Liu, S., W. Graham, and J. Jacobs (2005), Daily potential evapotranspiration and diurnal climate forcings: Influence on the numerical modeling of soil water dynamics and evapotranspiration, *J. Hydrol.*, *309*, 39–52.
Loveland, T. R., J. W. Merchant, B. C. Reed, J. F. Brown, D. O. Ohlen, P. Olson, and J. Hutchinson (1995), Seasonal land-cover regions of the United States, *Ann. Assoc. Am. Geogr.*, *85*, 339–355.
Meinke, I., J. Roads, and M. Kanamitsu (2007), Evaluation of RSM-simulated precipitation during CEOP, *J. Meteorol. Soc. Jpn.*, *85A*, 145–166.
Misra, V., P. Dirmeyer, and B. Kirtman (2003), Dynamical downscaling of seasonal simulations over South America, *J. Clim.*, *16*, 103–117.
Misra, V. (2007), Addressing the issue of systematic errors in a regional climate model, *J. Clim.*, *20*, 801–818.
Misra, V., and P. A. Dirmeyer (2009), Air, sea, and land interactions of the continental US hydroclimate, *J. Hydrometeorol.*, *10*, 353–373.
Misra, V., L. Moeller, L. Stefanova, S. Chan, J. J. O'Brien, T. J. Smith III, and N. Plant (2011), The influence of Atlantic warm pool on Panhandle Florida sea breeze, *J. Geophys. Res.*, *116*, D00Q06, doi:10.1029/2010JD015367.
Moorthi, S., and M. Suarez (1992), Relaxed Arakawa-Schubert: A parameterization of moist convection for general circulation models, *Mon. Weather Rev.*, *120*, 978–1002.
Parker, M. D., and D. A. Ahijevych (2007), Convective episodes in the east-central United States, *Mon. Weather Rev.*, *135*, 3707–3727.
Pielke, R. A. (1974), A three-dimensional numerical model of the sea breezes over South Florida, *Mon. Weather Rev.*, *102*, 115–139.
Portmann, R. W., S. Solomon, and G. C. Hegeri (2008), Spatial and seasonal patterns in climate change, temperatures, and precipitation across the United States, *Proc. Natl. Acad. Sci. U.S.A.*, *106*, 7324–7329, doi:10.1073/pnas0808533106.
Rayner, N. A., D. E. Parker, E. B. Horton, C. K. Folland, L. V. Alexander, D. P. Rowell, E. C. Kent, and A. Kaplan (2003), Global analyses of sea surface temperature, sea ice, and night marine air temperature since the late nineteenth century, *J. Geophys. Res.*, *108*(D14), 4407, doi:10.1029/2002JD002670.
Reynolds, R. W., N. A. Rayner, T. M. Smith, D. C. Stokes, and W. Wang (2002), An improved in situ and satellite SST analysis for climate, *J. Clim.*, *15*, 1609–1625.
Risbey, J. S., and P. H. Stone (1996), A case study of the adequacy of GCM simulations for input to regional climate change assessments, *J. Clim.*, *9*, 1441–1467.
Rogers, E., D. Deaven, and G. DiMego (1995), The regional analysis system for the operational "Early" eta model: Original 80-km configuration and recent changes, *Weather Forecasting*, *10*, 810–825.
Sapiano, M. R. P., and P. A. Arkin (2009), An intercomparison and validation of high-resolution satellite precipitation estimates with 3-hourly gauge data, *J. Hydrometeor.*, *10*, 149–166.
Schwartz, B. E., and L. F. Bosart (1979), The diurnal variability of Florida rainfall, *Mon. Weather Rev.*, *107*, 1535–1545.
Selman, C., V. Misra, L. Stefanova, S. DiNapoli, and T. J. Smith III (2013), Twenty-first-century wet season projections over the southeastern United States, *Reg. Env. Change.*, *13*, S153–164, doi:10.1007/s10113-013-0477-8.
Slingo, A., K. Hodges, and G. Robinson (2004), Simulation of the diurnal cycle in a climate model and its evaluation using data from Meteosat 7, *Q. J. R. Meteorol. Soc.*, *130*(599), 1449–1467.
Stefanova, L., V. Misra, S. Chan, J. J. O'Brien, and T. J. Smith III (2012), A proxy for high resolution regional reanalysis for the Southeast United States: Assessment of precipitation variability, *Clim. Dyn.*, *38*, doi:10.1007/s00382-011-1230-y.
Sun, G., S. G. McNulty, D. M. Amatya, R. W. Skaggs, L. W. Swift, J. P. Shepard, and H. Riekerk (2002), A comparison of the hydrology of the coastal forested wetlands/pine flatwoods and the mountainous uplands in the Southern US, *J. Hydrol.*, *263*, 92–104.

Tian, Y., C. D. Peters-Lidard, B. J. Choudhury, and M. Garcia (2007), Multitemporal analysis of TRMM-based satellite precipitation products for land data assimilation applications, *J. Hydrometeor.*, *8*, 1165–1183.

Uppala, S. M., et al (2005), The ERA-40 Re-analysis, *Q. J. R. Meteorol. Soc.*, *131*, 2961–3012, doi:10.1256/qj.04.176.

Wallace, J. M. (1975), Diurnal variations in precipitation and thunderstorm frequency over the conterminous United States, *Mon. Weather Rev.*, *103*, 406–419.

Wang, Y., L. Zhou, and K. Hamilton (2007), Effect of convective entrainment/detrainment on simulation of tropical precipitation diurnal cycle, *Mon. Weather Rev.*, *135*, 567–585.

Wei, J., and P. Dirmeyer (2012), Dissecting soil moisture-precipitation coupling, *Geophys. Res. Lett.*, *39*, L19711, doi:10.1029/2012GL053038.

Wootten, A., S. Raman, and A. Sims (2010), Diurnal variations of precipitation over the Carolina Sandhills Region, *J. Earth Syst. Sci.*, *119*, 579–596.

Wu, Z., N. Huang, J. Wallace, B. Smoliak, and X. Chen (2011), On the time-varying trend in global-mean surface temperature, *Clim. Dyn.*, *37*, 759–773.

Zhou, L., A. Dai, Y. Dai, R. S. Vose, C.-Z. Zou, Y. Tian, and H. Chen (2008), Spatial dependence of diurnal temperature range trends on precipitation from 1950 to 2004, *Clim. Dyn.*, *32*, 429–440.